Tuning Bulk O₂ and Nonbonding Oxygen State for Reversible Anionic Redox Chemistry in P2-Layered Cathodes

Zhenrui Li[1][‖], Weijin Kong[1][‖], Yang Yu[1], Jicheng Zhang[1], Deniz Wong[2], Zijian Xu[3], Zhenhua Chen[3], Christian Schulz[2], Maciej Bartkowiak[2] and Xiangfeng Liu[1,4]*

[1]Center of Materials Science and Optoelectronics Engineering, College of Materials Science and Optoelectronic Technology, University of Chinese Academy of Sciences, Beijing 100049, P. R. China.

[2]Helmholtz-Zentrum Berlin für Materialien und Energie, Hahn-Meitner-Platz 1, D-14109 Berlin, Germany.

[3]Shanghai Synchrotron Radiation Facility, Shanghai Institute of Applied Physics, Chinese Academy of Sciences, Shanghai 201204, P. R. China

[4]CAS Center for Excellence in Topological Quantum Computation, University of Chinese Academy of Sciences, Beijing 100190, China.

*Corresponding author. Email: liuxf@ucas.ac.cn

‖ These two authors contributed equally to this work.

TOC
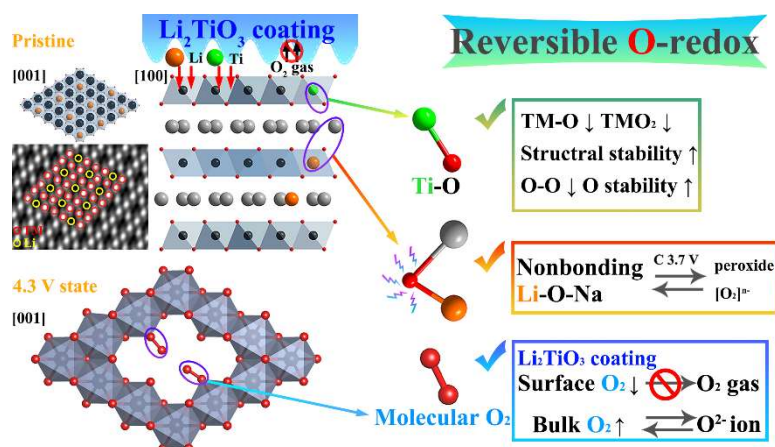
TOC Text:

How to improve the reversibility of O-redox chemistry is particularly important for P2-type layered cathodes in sodium ion batteries. Herein, we successfully tune bulk O_2 and nonbonding oxygen state for the reversible O-redox in P2-$Na_{0.67}Mn_{0.5}Fe_{0.5}O_2$ through a synergy of Li_2TiO_3 coating and Li/Ti co-doping. The underlying mechanism has been revealed by neutron diffraction, resonant inelastic X-ray scattering, density functional theory, etc.

Abstract

Improving the reversibility of oxygen redox is quite significant for layered oxides cathodes in sodium-ion batteries. Herein, we for the first time simultaneously tune bulk O_2 and nonbonding oxygen state for reversible oxygen redox chemistry in P2-$Na_{0.67}Mn_{0.5}Fe_{0.5}O_2$ through a synergy of Li_2TiO_3 coating and Li/Ti co-doping. O^{2-} is oxidized to molecular O_2 and peroxide $(O_2)^{n-}$ (n < 2) during charging. Molecular O_2 derived from transition metal (TM) migration is related to the superstructure ordering induced by Li doping. The synergy mechanism of Li_2TiO_3 coating and Li/Ti co-doping on the two O-redox modes is revealed. Firstly, Li_2TiO_3 coating restrains the surface O_2 and inhibits O_2 loss. Secondly, nonbonding Li-O-Na enhances the reversibility of $O^{2-}{\rightarrow}(O_2)^{n-}$. Thirdly, Ti doping strengthens the TM-O bond which fixes lattice oxygen. The cationic redox reversibility is also enhanced by Li/Ti co-doping. The proposed insights into the oxygen redox reversibility are insightful for other oxide cathodes.

Introduction

Sodium-ion batteries (SIBs) have attracted great interest due to the low cost and promising applications in large-scale energy storage.[1] A layered transition metal oxide cathode material is an important material for sodium-ion batteries.[2]. Oxygen redox in the layered cathode materials has been studied and proven to provide additional capacity during the charge and discharge process.[3] However, the oxygen redox process in SIBs can adversely affect the structure stability and reversible capacity of the cathode material.[4] Therefore, enhancing O-redox activity and reversibility is still a major challenge.

The oxygen-redox process has been extensively studied in Li-rich cathode materials since 2000. [5] Oxygen has been reported to provide additional capacity due to the nonbonding Li 2s-O 2p configuration.[6] A series of layered cathode materials for sodium-ion batteries with oxygen redox conditions, such as P2-$Na_{5/6}[Li_{1/4}Mn_{3/4}]O_2$ and P2-$Na_{0.6}[Li_{0.2}Mn_{0.8}]O_2$, were discovered.[7] A similar Li-O-Na configuration is also found in the materials with Li doping in transition metal (TM) layers.[8] Zhou et al. reported the stable Li-O-Na configuration in layered P2-type $Na_{0.66}Li_{0.22}Ru_{0.78}O_2$ cathode and achieved reversible anionic redox reactions.[9] The nonbonding Li-O-Na configuration has a band above the TM-O orbital bonding level.[10] The TM-O orbital in the bonding state is harmful to the structural stability of the cathode material in charge compensation process. However, nonbonding oxygen ions in the Li-O-Na configuration can maintain the structure stability of the cathode material during the charging/discharging process, thus improving the reversibility of the oxygen-redox chemistry in cathode materials.[11]

Recently, Bruce et al. discovered a new mechanism of the oxygen redox reaction in sodium- and lithium-ion batteries.[12]. Superstructure ordering is found in the TM layer when Li/Mg ions

enter the TM layer.[11b] The oxygen ions coordinated with one TM ion (O-TM1) tend to bond with oxygen ions not coordinated with TM ions (O-TM0), thus forming a Mn–η1–O2 moiety.[8] In this case, the TM vacancies attached to O_2 species are linked together in spatial arrangement due to the migration of transition metals, thus forming vacancy clusters. The O_2 species are molecular O_2 trapped in vacancy clusters in the material. Molecular O_2 is also present in a variety of cathode materials, such as P2-$Na_{0.75}Li_{0.25}Mn_{0.75}O_2$,[8] P2-$Na_{0.67}Mn_{0.72}Mg_{0.28}O_2$,[12d] $Li_{1.2}Ni_{0.13}Co_{0.13}Mn_{0.54}O_2$,[12b] and Li_2MnO_2F[12c]. Molecular O_2 can be generated in bulk or on the surface of the cathode material. Bulk O_2 is stably trapped in the vacancy cluster in the deep bulk of the material, while surface O_2 is easily lost in charge and discharge processes. It is well known that surface modification can inhibit the production of molecular O_2 on the material surface and further reduce gaseous O_2 release and oxygen loss, which improves the stability of oxygen redox.[12a] However, the molecular O_2 mechanism has not been clearly discussed in various sodium-ion layered cathode materials, and oxygen release inhibition by the mechanism has not been deeply understood.

Herein, we simultaneously tune bulk O_2 and the nonbonding oxygen state for reversible anionic redox chemistry in P2-type $Na_{0.67}Mn_{0.5}Fe_{0.5}O_2$ (MF) cathode material for the first time by Li_2TiO_3 coating and Li/Ti co-doping. The modified sample is abbreviated as LTO@MF. The O-redox process and the modulation mechanism are revealed by a combination of some advanced analytical techniques (neutron diffraction, Resonant inelastic X-ray scattering, high-angle annular dark-field scanning transmission electron microscopy, O K-edge soft X-ray absorption spectroscopy and so on) and calculations. Li_2TiO_3 coating restrains the surface O_2 and inhibits O_2 loss, and nonbonding Li-O-Na enhances the reversibility of $O^{2-} \rightarrow (O_2)^{n-}$. Ti doping also strengthens the TM-O bond thus

fixing lattice oxygen. This study offers some new insights into tuning the reversibility of oxygen

anion redox chemistry.

Results and discussion

1. Role of coating and co-doping synergy
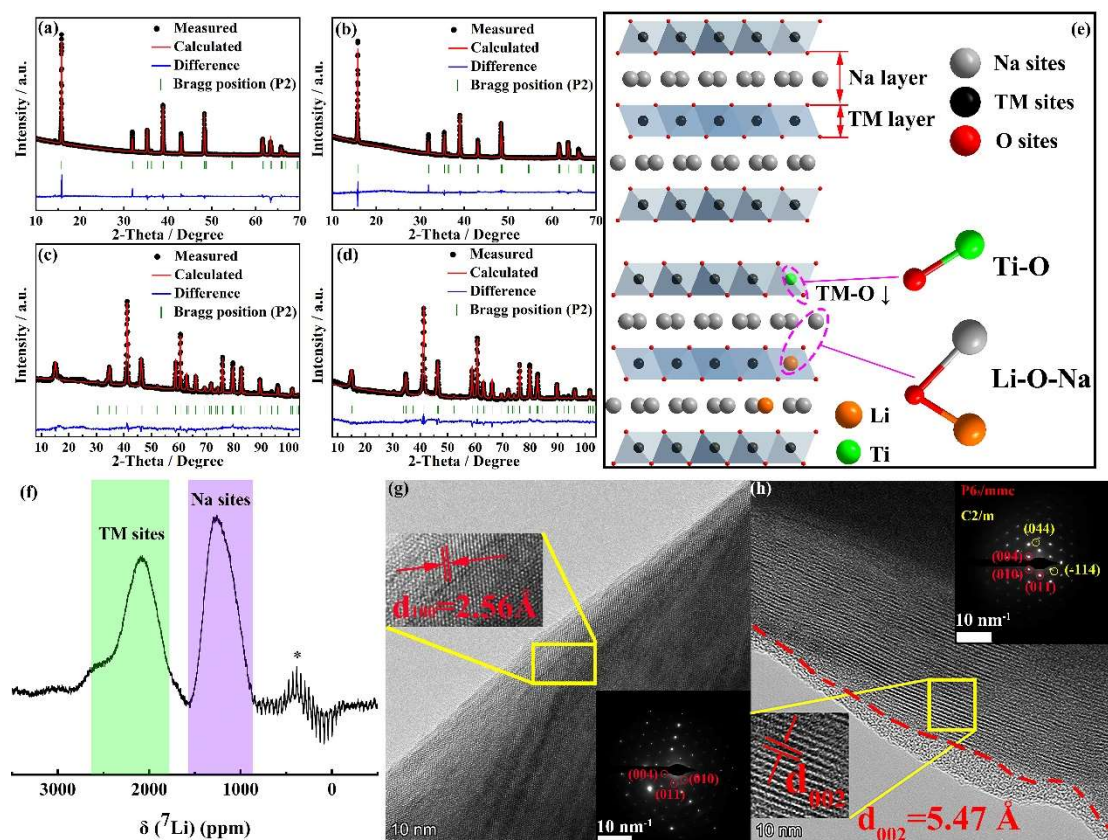
Figure 1. Structure and morphology of MF and LTO@MF materials. XRD refinement results of (a) MF and (b) LTO@MF. Neutron powder diffraction refinement results of (c) MF and (d) LTO@MF. (e) Crystal structure of the P2-type MF (up) and LTO@MF (down) samples. (f) ^{7}Li MAS solid state NMR (ssNMR) data of pristine LTO@MF. HR-TEM and SAED images of (g) MF and (h) LTO@MF.

XRD refinement results and neutron powder diffraction (NPD) refinement results of MF and

LTO@MF samples (Figure 1(a)-(d)) presents the P6$_3$/mmc space group (No 194).[13] NPD results

demonstrate that Li is doped into Nae and TM sites, and Ti is doped into TM sites in the LTO@MF

sample, as shown in Figure 1(d) and Table S5. From XRD results in Figure S1(a), compared with

the MF sample, the (002) peak shift of TiO$_2$@MF, NTO@MF, LTO@MF toward a lower angle

(Figure S1(b)) represents an increase in lattice parameter c (Table S3, S6), which indicates the expansion of the (002) slab.[14] Ti may tend to enter the TM octahedral sites and bond with O. The Ti-O bonding energy (662 kJ mol^{-1}) is larger than Mn-O (402 kJ mol^{-1}) and Fe-O (409 kJ mol^{-1}), resulting in the shrinkage of O-O, TM-O bond length and TMO_2 thickness, which benefits the stability of O.[15] The increase in Na-O and d indicates that the Na diffusion channel is enlarged in LTO@MF sample, which enhances the rate capacity. ^{7}Li MAS ss-NMR is sensitive to Li ions in different environments and is hence applied to determine the specific Li doping sites in LTO@MF samples.[14a, 16] As presented in Figure 1(f), the ^{7}Li resonances around chemical shifts presented with green and purple regions are assigned to Li in TM and Na sites, respectively.[14a, 14b, 17] It can be confirmed that Li ions enter the TM sites, and there may be a small amount of Li occupying Na position. For Li in TM sites, the low orbital overlapping of Li 2s and O 2p can form the Li-O-Na configuration with a higher Fermi level than other TM-O bonding levels, leading to higher anionic redox capacity and reversibility.[6, 10b, 18] The above discussion of the crystal structure is shown in Figure 1(e).

The morphology of the MF and LTO@MF samples was characterized by HR-TEM (Figure 1(g) and (h)), SEM (Figure S2(d) and (e)), EDS mapping (Figure S2(b) and (c)) and STEM (Figure S2(a)). The cationic and anionic element valence states of the MF and LTO@MF samples were characterized by XPS as shown in Figure S3. The lattice and surface O peaks were fitted as shown in Figure S3(b).[19] From Table S8, the improvement of the lattice O ratio in LTO@MF was caused by the enhancement of the TM-O bonding energy due to Ti doping, which is beneficial for O-redox reversibility and structural stability.
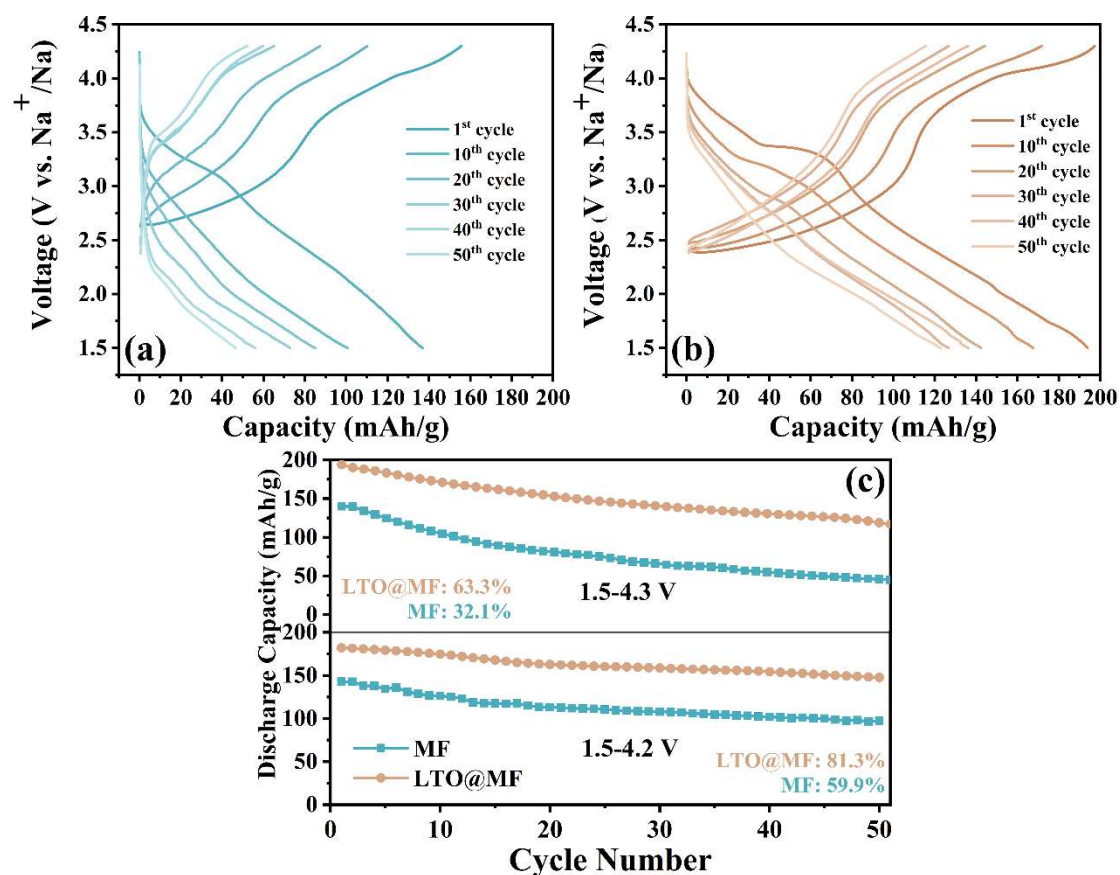
Figure 2. Capacity-voltage curves from 1.5-4.3 V at 0.1C of (a) MF and (b) LTO@MF for different cycle numbers. (c) Cycling performance for the MF and LTO@MF samples performed in two voltage ranges of 1.5-4.3 V and 1.5-4.2 V.

The rate performance of the bare MF and the samples coated with TiO_2, Li_2TiO_3 (LTO) and Na_2TiO_3 samples in a voltage range of 1.5-4.2 V has been shown in Figure S4(a). Among all samples, the LTO@MF sample presents the best rate performance, revealing that the Li_2TiO_3 (LTO) coating strategy can improve the rate performance more effectively. The improved rate performance of LTO@MF is due to the expansion of Na layer, which is presented in Table S3. As shown in Figure S5, GITT results shows that the Na$^+$ diffusion coefficients of the LTO@MF sample are larger than those of the MF sample, demonstrating the faster sodium diffusion kinetics in the LTO@MF sample due to the expanded Na layer, leading to the improvement of the rate performance in the LTO@MF sample.

As shown in Figure 2, the cycling performance was presented for MF and LTO@MF samples. The charge/discharge curves for the MF and LTO@MF samples of 1.5-4.3 V are presented in Figure 2(a) and (b), respectively. In the 50th cycle, the voltage of the MF sample drops below 2.5 V at the beginning of discharge, while only drops to 3.5 V in the LTO@MF sample, indicating voltage decay is reduced in the LTO@MF sample, which is caused by the reversible O-reduction process. Figure 2(c) shows the cycling results of both samples at 0.1 C in voltage range of 1.5-4.2 V and 1.5-4.3 V. When the voltage increases from 4.2 V to 4.3 V, the first cycle capacity of the LTO@MF material rises from 182.0 mAh/g to 193.9 mAh/g, while those of the MF sample are 142.8 and 140.1 mAh/g, respectively. The increasing capacity of the LTO@MF sample is caused by the excitation of more O-redox at higher voltage. The additional capacity for the LTO@MF material is due to the high-energy Li 2s-O 2p configuration,[6, 10] which is discussed in the following sections. The capacity retentions of the LTO@MF sample (81.3% of 1.5-4.2 V and 63.3% of 1.5-4.3 V) are increased compared with MF sample (59.9% of 1.5-4.2 V and 32.1% of 1.5-4.3 V). In addition, the cyclic performance at 1 C and 0.5 C is also enhanced in LTO@MF sample as shown in Figure S4(b) and (c). Therefore, the synergistic modification strategy improves the electrochemical performance of the material.

Ex situ XPS Mn 2p results are presented in Figure S6. The change in Mn^{3+}/Mn^{4+} under various charge and discharge voltages is analyzed in Table S9. The relative content of Mn^{3+} for the LTO@MF sample is lower than that of the MF sample, which proves the inhibition of Mn^{3+} content and the harmful Jahn-Teller effect. For LTO@MF sample, the reversible cationic redox process is proved by the change of Mn valence states during charge and discharge. *Ex situ/in situ* XRD results show the change ratios of lattice parameters at different voltages as illustrated in Table S5 and Figure

S7. In addition, the variation of lattice parameters and HR-TEM results for both samples before and

after 100 cycles is presented in Table S11 and Figure S8, further confirming the enhancement of

structural stability in the LTO@MF sample.

2. Enhancement of O-redox reversibility
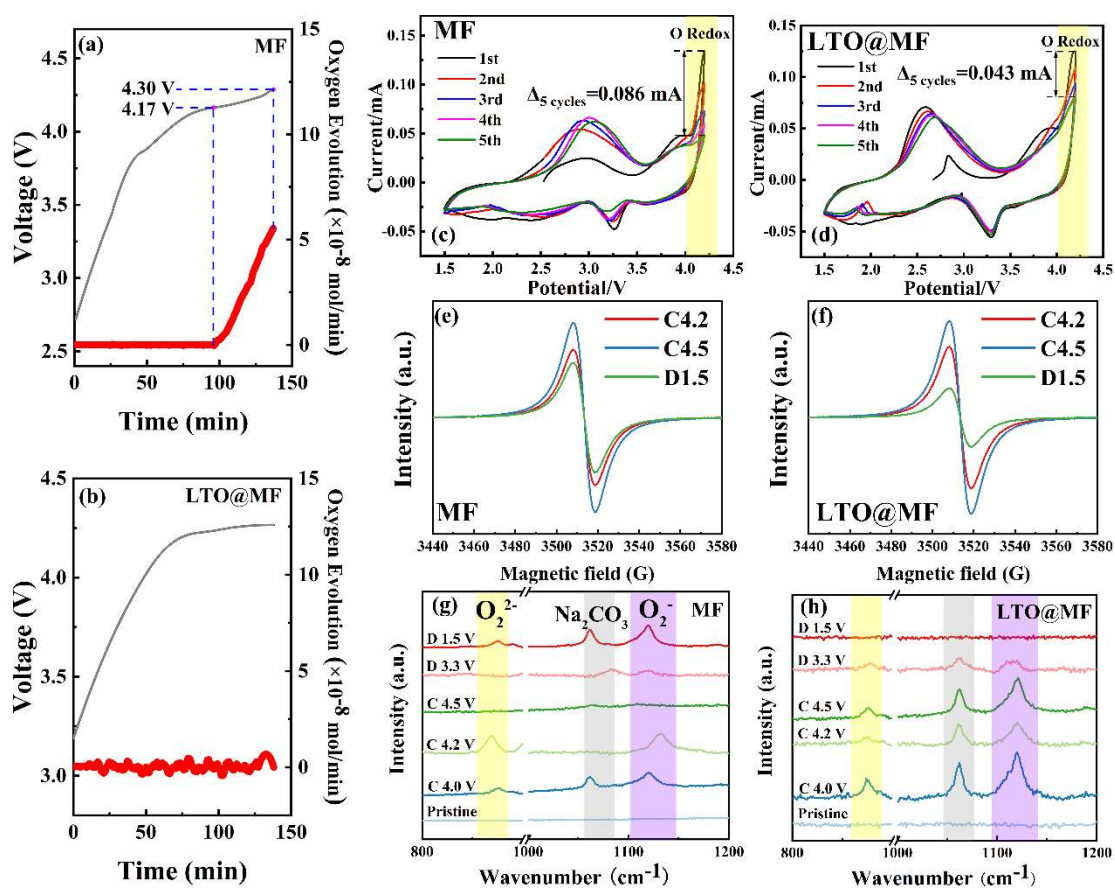
Figure 3. DEMS results and corresponding charge curves of (a) MF sample and (b) LTO@MF sample. 1.5-4.2 V CV curves: (c) MF sample and (d) LTO@MF sample. *Ex situ* EPR results of (e) MF sample and (f) LTO@MF sample. *Ex situ* Raman spectra results of (g) MF material and (h) LTO@MF material. Yellow, purple and grey regions are assigned to peroxide, superoxide related O-O and Na2CO3 derived from surface passivation.

The regulation of the O-redox process plays a key role in improving the electrochemical

performance in the LTO@MF material. Therefore, a series of experiments were applied to explore

the O-redox process in both cathodes. E*x situ* XPS O 1s results was applied to reveal the relative

content of different O species during the charge/discharge process, as shown in Figure S6(c)-(f) and

Table S10.[14c, 19] The existence of O_2^{2-} reveals that the O ions are oxidized and contribute a capacity during charging.[20]

DEMS can detect very small amounts of gaseous O_2 produced by the material during the charge/discharge process.[11b, 21] The DEMS test is conducted from 1.5 V to 4.3 V at 0.5 C during the first cycle. As shown in Figure 3(a), O release is observed in the MF sample in the voltage range of 4.17-4.30 V, which is consistent with O being oxidized at high voltage.[9] The O release of the MF sample proves the irreversible O oxidation in the MF sample. However, no O release is observed in the LTO@MF sample as shown in Figure 3(b). It can be confirmed that the irreversible O_2 release was prevented at high voltage.

CV tests were applied for both MF and LTO@MF materials at a scan rate of 0.1 mV/s. Figure 3(c) and (d) presents the CV result of 1.5-4.2 V for MF and LTO@MF samples, respectively. The Mn oxidation peak (2.5836 V) and the Fe reduction peak (3.2989 V) of LTO@MF overlaps well after cycling, which reveals the improved cyclic stability. In addition, polarization was lowered and the cationic redox reversibility was enhanced in the LTO@MF sample. The oxidation peak above 4.0 V corresponds to O-oxidation process.[22] For the MF sample, the reduction in peak intensity involving O oxidation after 5 cycles greater than that of the LTO@MF sample. The O-oxidation peak of the 5th cycle for the MF sample is almost invisible, while was clearly identified for the LTO@MF sample revealing the enhancement of O-redox reversibility in the LTO@MF sample. The O loss of MF at high voltage leads to a decrease in O ions, which results in a rapid O-redox reduction in the following cycles.

EPR test was performed to characterize the electronic states of O ions under perpendicular mode.[23] Figure S10 shows that the broad centrosymmetric peak shape corresponds to the coupling

of tetravalent manganese and O ions.[24] After charging to high voltage, the Mn-O bonding becomes weak due to O-oxidation. Therefore, the former broad peak disappeared, and a new sharp line shape from 3480-3540 G assigned to high valence O_2^{n-} ($n \leq 2$) species with single unpaired electrons appeared.[14b, 25] The O_2^{n-} signals are enlarged in Figures 3(e) and (f) for both MF and LTO@MF samples, respectively. For MF and LTO@MF samples, the resonance intensity increases from C4.2 to C4.5 V and decreases from C4.5 V to D1.5 V, which reveals that the amount of O_2^{n-} species increases during the charging process and decreases during the discharging process. However, the peak of D1.5 maintains a high level near the peak of C4.2 in the MF sample, while the D1.5 peak presents lower intensity than C4.2 peak in the LTO@MF sample. This means that O_2^{n-} in the LTO@MF material is reduced to O^{2-}, but not in the MF sample, which proves the improvement of O-redox reversibility in the LTO@MF sample. Figure S11(a) and (b) show the EPR results of fully charged MF and LTO@MF after various cycles. The higher O_2^{n-} intensity in the LTO@MF sample demonstrate a reversible O-redox process without O loss.

Raman spectroscopy can detect the O-O stretch information in the bulk structure of the materials (≈ 1 μm) [9] *Ex situ* Raman results are presented in Figure 3(g) and (h) for MF and LTO@MF materials, respectively. The O-O stretch at 850 cm^{-1} and 1150 cm^{-1} can be ascribed to peroxide-related O_2^{2-} and superoxide-related O_2^-, respectively.[26] The signal of Na_2CO_3 species derived from the electrolyte decomposition is also observed. As shown in Figure 3(g), O_2^{2-} and O_2^- stretching modes are observed in the MF sample at the 4.2 V state, which reveals that O is oxidized to high valence. The O_2^{2-} and O_2^- species disappear at 4.5 V because most O_2^{n-} species are oxidized to higher valence and lost as O_2 gas. When discharging to 1.5 V, the residual O species at high valence is reduced to O_2^{n-} species. The existence of O_2^{2-} and O_2^- species after discharge to 1.5 V can

be oxidized easily to O_2 gas, which indicates the irreversible O-redox process in the MF material.

Figure 3(h) presents *ex situ* Raman results of the LTO@MF sample. When charging to 4.5 V, the existence of O_2^{2-} and O_2^- species reveals the O-oxidation process. Then, the O_2^{2-} and O_2^- species disappear at discharging the 1.5 V state, which illustrates a reversible O-redox process of the LTO@MF sample. The Raman results of the MF and LTO@MF samples after 30 and 50 cycles are shown in Figure S11(c). O_2^{2-} or O_2^- stretches are not observed in the MF sample but clearly identified in the LTO@MF sample, revealing that the O loss leads to irreversible O-redox in the MF sample. A detailed analysis of O species in O-redox is given in the next section.

3. Molecular O_2 and peroxide/superoxide $(O_2)^{n-}$
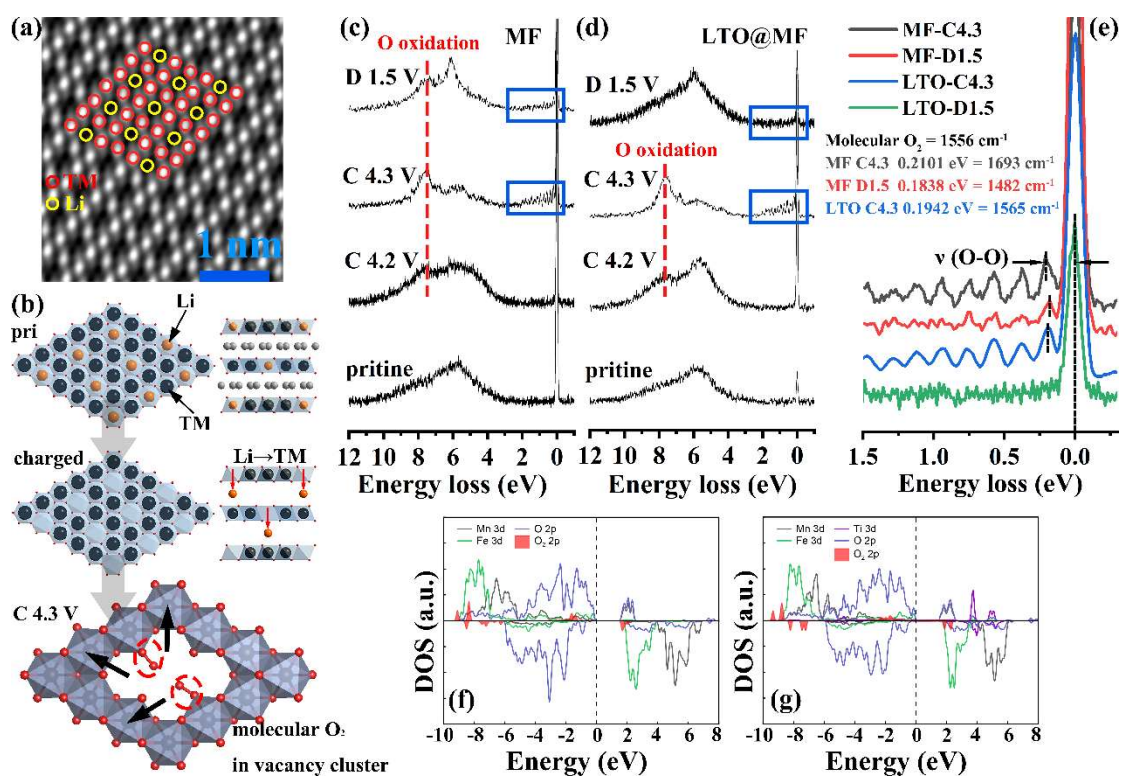
Figure 4. (a) HAADF-STEM image collected at a surface depth of 30 nm in the pristine LTO@MF sample viewing along [001] perpendicular to ab plane. (b) Schematic of molecular O_2 formation in a TM vacancy cluster. O K-edge RIXS results at 531.0 eV of (c) MF and (d) LTO@MF samples. (e) Enlargement of a series of elastic peaks marked by blue rectangles in figure 4c and d. DOS results from DFT calculation for (f) MF and (g) LTO@MF samples charged to 4.3 V. Red shading represents electron holes on molecular O_2.

According to previous works, with superstructure ordering from Li/Mg in TM layers, the

migration of Li and Mn ions during charging forms the molecular O_2. [8, 12, 27] Figure 4(a) shows the STEM image of the pristine LTO@MF sample at a surface depth of 30 nm viewed along [001] direction. Since the detecting depth is greater than the thickness of the coating layer, it can be confirmed that the observed lattice belongs to the P2-layered oxide. By a focused ion beam (FIB), a single layer of TM ions is shown in the image. The bright white spots with red circles are TM ions. The black holes with yellow circles in the center of six TM ions represent the Li in TM sites. The regular distribution of Li in the TM layer proves the superstructure ordering in the LTO@MF material. Since Li is only distributed in a certain range of surface depths, the superstructure ordering is not observed by STEM above 100 nm depth, as shown in Figure S2(a). The limited content of superstructure ordering makes it not detected by XRD. In addition, as shown in Figure S13, no superstructure ordering is observed viewed along the [100], since the dark spots (Li) are covered by the bright spots (TM) in the next layer. The atomic arrangement is different from that in the previous research.[12a] Its formation mechanism needs further study.

From the superstructure ordering, a model of the TM layer with Li arrangement for the LTO@MF sample is constructed in Figure 4(b). According to previous work,[8, 12b] we infer a possible TM migration mode during charging, leading to molecular O_2 bonding to TM in the vacancy cluster, as shown in Figure 4(b). By DFT, we calculated a stable model of a vacancy cluster containing four TM vacancies and two molecular O_2 for MF (-332.37 meV/f.u.) and LTO@MF (-329.91 meV/f.u.) charging to 4.3 V in Figure 4(b). As shown in Figure 4(f) and (g), the DOS results of MF and LTO@MF samples present the electron holes on O_2 2p orbitals. The calculated O-O bonds in the O_2 configurations for the MF and LTO@MF samples are 1.21 and 1.22 Å, respectively, which is consistent with the molecular O_2 bond length of 1.20 Å.[12c, 28] Therefore, the calculation

results predict the molecular O_2 in charged materials.

The *ex-situ* O K-edge RIXS results for MF and LTO@MF samples are presented in Figure 4(c) and (d), respectively. An inelastic peak at approximately 7.5 eV represents the O-oxidation in charged MF and LTO@MF samples.[29] When discharging to 1.5 V, the inelastic peak was still observed in the MF sample but not in the LTO@MF sample. The blue rectangles highlight the region of low-energy elastic peaks associated with O-O vibration for C4.3 V and D1.5 V states of the MF samples, while only present in C4.3 V state of LTO@MF material. From an enlarged picture of the elastic peaks in Figure 4(e), the obtained vibrational frequencies for MF-C4.3 V, MF-D1.5V and LTO-C4.3V materials are 1693, 1482, and 1565 cm^{-1}, respectively. The fundamental vibrational frequency of molecular O_2 is 1556 cm^{-1},[12b, 12d] gaseous O_2 is 1600 cm^{-1}, and peroxide $(O_2)^{2-}$ and superoxide $(O_2)^-$ are 790 and 1100 cm^{-1}, respectively.[28a, 30] The O species observed from RIXS elastic peaks are assigned to molecular O_2. From Figure. S15 (a) and (b), *ex situ* Raman results shows that the molecular O_2 signals are observed at approximately 1500-1550 cm^{-1} for MF in the C4.2 V, C4.3 V, D1.5 V states, and LTO@MF in the C4.3 V state, which is consistent with the *ex situ* RIXS results.

The O-redox process from RIXS results is analyzed in detail. The larger fundamental vibrational frequency of the MF sample (1693 cm^{-1}) than that of the LTO@MF sample (1565 cm^{-1}) at 4.3 V state, proves the bond between the molecular O_2 and TM in the lattice is weaker for MF sample.[8, 28a] In the MF-C4.3V sample, the molecular O_2 is closer to the gaseous oxygen state. This indicates that the O-oxidation degree in MF sample is higher than that in LTO@MF sample. From *ex situ* Raman result of MF sample in Figure 3(g), when charging to 4.5 V, most peroxide and superoxide species were oxidized to higher valence species, and ultimately forming gaseous O_2,

resulting in irreversible O-redox process. However, RIXS result of LTO@MF-C4.3V sample shows strengthened interaction between molecular O_2 and the lattice TM, and plenty of O still remains in peroxide and superoxide species at C4.5V state (Figure 3(h)) without O_2 gas release. When discharging to 1.5 V, the elastic peaks assigned to molecular O_2 can still be observed in the MF sample but not in the LTO@MF sample, as shown in Figure 4(e). In MF sample, after O_2 gas releasing, the remaining molecular O_2 weakly bonded to the lattice is gradually reduced. From MF-D1.5V RIXS result (Figure 4(c) and (e)), the vibration frequency of molecular O_2 decreases from 1693 to 1482 cm^{-1}, showing that the bond between O and lattice is enhanced. Eventually, part of the molecular O_2 in MF-D1.5V sample is reduced to peroxide and superoxide as shown in Raman results (Figure 3(g)), but there is still some molecular O_2, which is not reduced (Figure 4(c) and (e)), proving the irreversible O-redox process in MF sample. The RIXS inelastic peak at 7.5 eV for MF-D1.5V sample also demonstrate that O species in high valence have not been completely reduced. For LTO@MF-D1.5V sample, no signal of molecular O_2 and peroxide/superoxide species is observed in RIXS results (Figure 4(d) and (e)) and Raman (Figure 3(h)), and the RIXS inelastic peak is not observed, which reveals that the molecular O_2 in LTO@MF has been reduced to initial O^{2-}, demonstrating the reversible O-redox process in LTO@MF sample.

Molecular O_2 in bulk material is stable and can be reversibly reduced to O^{2-}, while on the material surface it is easily lost in charge and discharge processes.[8, 12a] From DEMS and RIXS results, a part of the surface O_2 in the MF sample turned into O_2 gas during the first cycle. The remaining surface O_2 was not reduced to O^{2-} and could escape as O_2 gas in the next cycle. Due to surface modification, the surface O_2 is inhibited in the LTO@MF sample, thus promoting the reversible O-redox process.[12b]
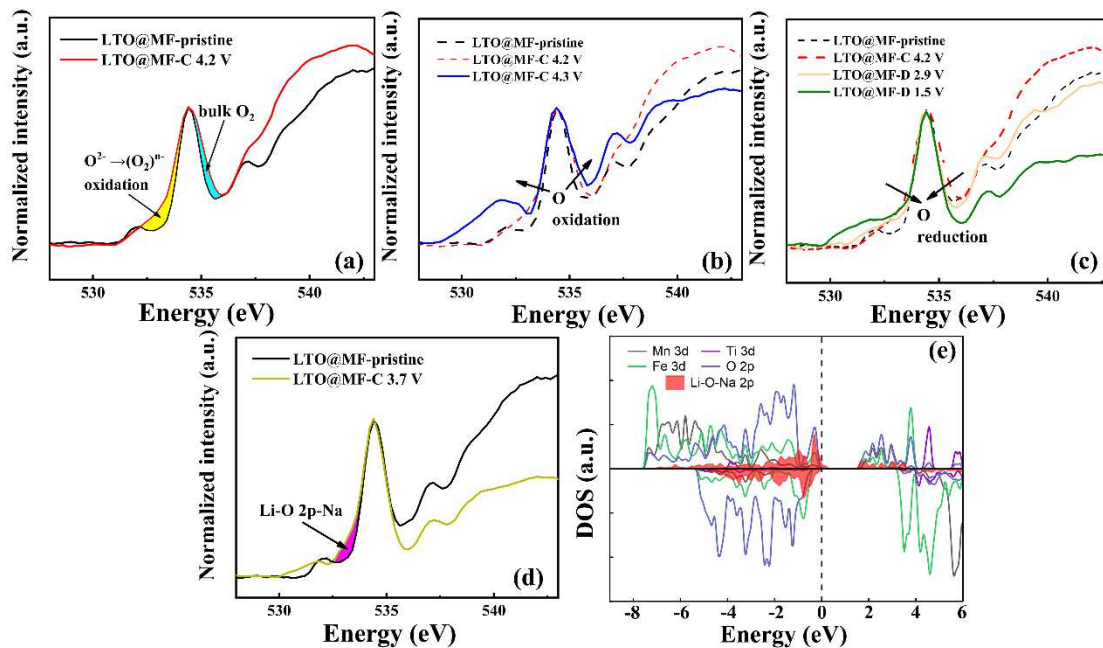
Figure 5. (a) Redox process shown by O K-edge soft XAS in TEY mode results of LTO@MF sample. *Ex situ* sXAS results of LTO@MF sample during (b) charging and (c) discharging process. (d) sXAS results of LTO@MF sample at pristine and charging to 3.7 V states. (e) DOS plots from DFT calculation of pristine LTO@MF material.

Figure 5(a) shows the O K-edge soft XAS results for the LTO@MF sample of pristine material charging to 4.2 V states. The integral areas of the sXAS pre-edge represent different O-oxidation systems. The change in the region between excitation energies of 532-534 eV (yellow) represents the oxidation process from O^{2-} to peroxide/superoxide $(O_2)^{n-}$ (n<2).[8, 12d] The integral areas between 534-536 eV (blue) represent the oxidation process from O^{2-} to molecular O_2.[12b] From Figure 5(a), it can be found that O^{2-} in the LTO@MF sample were oxidized to both $(O_2)^{n-}$ (n<2) species and molecular O_2 when charging to 4.2 V. Figure S12(a) and Figure 5(b) present the sXAS results during the charging process, revealing O^{2-} oxidation to both $(O_2)^{n-}$ (n<2) species and molecular O_2 in both samples. Figure S12(b) and Figure 5(c) present the sXAS results during the discharging process, indicating the O-reduction process. In Figure 5(c), the sXAS pattern in the 534-536 eV region for the LTO@MF material overlaps well after the first cycling, illustrating that the molecular O_2 is reduced to O^{2-} during the discharging process. [8, 12a]

The energy of the Li-O-Na structure was higher than that of other TM-O structures, due to the nonhybridized O 2p orbitals,[18] which improves the specific capacity and the anionic redox reversibility.[11c, 12b] Li in TM sites can form the Li-O-Na configuration in LTO@MF cathode. The plateau in Figure 2(b) of 3.5-4.0 V during charging may involve nonbonding Li-O-Na in the LTO@MF sample. Figure 5(d) and Figure S12(c) show the sXAS results of LTO@MF and MF at pristine and C3.7V states, respectively. Integral areas (purple) representing O-oxidation involving nonbonding Li-O-Na at C3.7 V are observed in the LTO@MF sample but not in the MF sample.[12b, 22] Figure 5(e) shows the DOS plots of the pristine LTO@MF material obtained by DFT calculations. Among all the cationic and anionic orbitals, the O 2p orbital contributes the most below the Fermi level. In addition, most of the O 2p orbitals are composed of Li-O-Na structures, indicating that the Li-O-Na configuration produces a preferential O-redox reaction.[11c] In summary, the nonbonding Li-O-Na configuration enhances peroxide/superoxide related O-redox reversibility.

Conclusion

Molecular O_2 and peroxide/superoxide $(O_2)^{n-}$ species were detected in P2-type $Na_{0.67}Mn_{0.5}Fe_{0.5}O_2$ cathode material and modified by a Li_2TiO_3 coating and Li/Ti co-doping synergic strategy. The oxygen redox mechanism has been revealed. Oxygen ions are oxidized to molecular O_2 and peroxide/superoxide $(O_2)^{n-}$ species. Molecular O_2 is generated due to the superstructure derived from Li substitution. During the charging process, Li migrates from the TM layer to the Na layer, and other TM ions undergo in plain migration to form molecular O_2 trapped in vacancy clusters. According to the above two oxygen redox modes, we unveiled the following synergy mechanism of Li_2TiO_3 coating and Li and Ti co-doping. 1) The coating modification inhibited the formation of molecular O_2 on the surface, and gaseous oxygen loss was prevented in the modified

sample. 2) Li substitution in transition metal sites will form a nonbonding Li-O-Na configuration, which improves the reversibility of the oxygen redox between oxygen ions and peroxide $(O_2)^{n-}$ species. 3) Ti substitution also increases the bonding energy between transition metal ions and oxygen ions, which is beneficial to improving specific capacity and anionic redox reversibility. The reversible oxygen redox chemistry reduces the voltage decay and increases the reversible capacity of the material. In addition, the regulation of the lattice structure and the reversible cationic chemistry are also clarified. The modified sample delivers a highly reversible specific capacity of 147.8 mAh/g with 63.3% capacity retention in a voltage window of 1.5-4.3 V after 50 cycles. More broadly, this study detects the coexisting molecular O_2 and peroxide/superoxide $(O_2)^{n-}$ species generated from oxygen oxidation in P2-layered cathodes and first regulates both oxygen redox systems simultaneously. Further research is required to explore the specific mechanisms of different oxygen oxidation species in other cathode materials, which is critical in the precise modulation of oxygen redox chemistry. In addition, this proposed synergetic strategy can also provide ideas to improve the cyclic stability and specific capacity of layered cathode materials.

Acknowledgements

at China Advanced Research Reactor (CARR) and School of Physics, Peking University for the

neutron powder diffraction testing.

References

[1] N. Yabuuchi, K. Kubota, M. Dahbi, S. Komaba, *Chem. Rev.* **2014**, *114*, 11636-11682.

[2] a) P. F. Wang, Y. You, Y.X. Yin, Y. G. Guo, *Adv. Energy Mater.* **2018**, *8*, 1701912; b) Q. Liu, Z. Hu, W. Li, C. Zou, H. Jin, S. Wang, S. Chou, S. X. Dou, *Energy Environ. Sci.* **2021**, *14*, 158-179.

[3] a) M. Ben Yahia, J. Vergnet, M. Saubanere, M. L. Doublet, *Nat. Mater.* **2019**, *18*, 496–502; b) D. Kim, M. Cho, K. Cho, *Adv. Mater.* **2017**, *29*, 1701788; c) C. Ma, J. Alvarado, J. Xu, R. J. Clement, M. Kodur, W. Tong, C. P. Grey, Y. S. Meng, *J. Am. Chem. Soc.* **2017**, *139*, 4835-4845.

[4] a) M. Sathiya, A. M. Abakumov, D. Foix, G. Rousse, K. Ramesha, M. Saubanere, M. L. Doublet, H. Vezin, C. P. Laisa, A. S. Prakash, D. Gonbeau, G. VanTendeloo, J. M. Tarascon, *Nat. Mater.* **2015**, *14*, 230-238; b) P. Zheng, J. Su, Y. Wang, W. Zhou, J. Song, Q. Su, N. Reeves-McLaren, S. Guo, *Chemsuschem* **2020**, *13*, 1793-1799.

[5] a) M. Sathiya, G. Rousse, K. Ramesha, C. P. Laisa, H. Vezin, M. T. Sougrati, M. L. Doublet, D. Foix, D. Gonbeau, W. Walker, A. S. Prakash, M. Ben Hassine, L. Dupont, J. M. Tarascon, *Nat. Mater.* **2013**, *12*, 827-835; b) E. McCalla, A. M. Abakumov, M. Saubanere, D. Foix, E. J. Berg, G. Rousse, M. L. Doublet, D. Gonbeau, P. Novak, G. Van Tendeloo, R. Dominko, J. M. Tarascon, *Science* **2015**, *350*, 1516-1521; c) W. S. Yoon, M. Balasubramanian, K. Y. Chung, X. Q. Yang, J. McBreen, C. P. Grey, D. A. Fischer, *J. Am. Chem. Soc.* **2005**, *127*, 17479-17487.

[6] D. H. Seo, J. Lee, A. Urban, R. Malik, S. Kang, G. Ceder, *Nat. Chem.* **2016**, *8*, 692-697.

[7] a) N. Yabuuchi, R. Hara, M. Kajiyama, K. Kubota, T. Ishigaki, A. Hoshikawa, S. Komaba, *Adv. Energy Mater.* **2014**, *4*, 1301453; b) E. de la Llave, E. Talaie, E. Levi, P. K. Nayak, M. Dixit, P. T. Rao, P. Hartmann, F. Chesneau, D. T. Major, M. Greenstein, D. Aurbach, L. F. Nazar, *Chem. Mater.* **2016**, *28*, 9064-9076.

[8] R. A. House, U. Maitra, M. A. Perez-Osorio, J. G. Lozano, L. Jin, J. W. Somerville, L. C. Duda, A. Nag, A. Walters, K.-J. Zhou, M. R. Roberts, P. G. Bruce, *Nature* **2020**, *577*, 502–508.

[9] X. Cao, H. Li, Y. Qiao, X. Li, M. Jia, J. Cabana, H. Zhou, *Adv. Energy Mater.* **2020**, *10*, 1903785.

[10] a) H. Xu, S. Guo, H. Zhou, *J. Mater. Chem. A* **2019**, *7*, 23662-23678; b) G. Assat, J. M. Tarascon, *Nat. Energy* **2018**, *3*, 373-386.

[11] a) N. Yabuuchi, R. Hara, K. Kubota, J. Paulsen, S. Kumakura, S. Komaba, *J. Mater. Chem. A* **2014**, *2*, 16851-16855; b) U. Maitra, R. A. House, J. W. Somerville, N. Tapia-Ruiz, J. G. Lozano, N. Guerrini, R. Hao, K. Luo, L. Jin, M. A. Pérez-Osorio, F. Massel, D. M. Pickup, S. Ramos, X. Lu, D. E. McNally, A. V. Chadwick, F. Giustino, T. Schmitt, L. C. Duda, M. R. Roberts, P. G. Bruce, *Nat. Chem.* **2018**, *10*, 288-295; c) B. M. de Boisse, S.-i. Nishimura, E. Watanabe, L. Lander, A. Tsuchimoto, J. Kikkawa, E. Kobayashi, D. Asakura, M. Okubo, A. Yamada, *Adv. Energy Mater.* **2018**, *8*, 1800409; d) Q. C. Wang, J. K. Meng, X. Y. Yue, Q. Q. Qiu, Y. Song, X. J. Wu, Z. W. Fu, Y. Y. Xia, Z. Shadike, J. Wu, X. Q. Yang, Y. N. Zhou, *J. Am. Chem. Soc.* **2019**, *141*, 840-848.

[12] a) R. A. House, J. J. Marie, M. A. Perez-Osorio, G. J. Rees, E. Boivin, P. G. Bruce, *Nat. Energy* **2021**, *6*, 781–789; b) R. A. House, G. J. Rees, M. A. Pérez-Osorio, J. J. Marie, E. Boivin, A. W. Robertson, A. Nag, M. Garcia-Fernandez, K. J. Zhou, P. G. Bruce, *Nat. Energy* **2020**, *5*, 777-785; c) R. Sharpe, R. A. House, M. J. Clarke, D. Förstermann, J. J. Marie, G. Cibin, K. J. Zhou, H. Y.

Playford, P. G. Bruce, M. S. Islam, *J. Am. Chem. Soc.* **2020**, *142*, 21799-21809; d) E. Boivin, R. A. House, M. A. Pérez-Osorio, J. J. Marie, U. Maitra, G. J. Rees, P. G. Bruce, *Joule* **2021**, *5*, 1267-1280.

[13] P. F. Wang, Y. You, Y. X. Yin, Y. S. Wang, L. J. Wan, L. Gu, Y. G. Guo, *Angew. Chem. Intern. Ed.* **2016**, *55*, 7445-7449.

[14] a) L. Yang, X. Li, J. Liu, S. Xiong, X. Ma, P. Liu, J. Bai, W. Xu, Y. Tang, Y. Y. Hu, M. Liu, H. Chen, *J. Am. Chem. Soc.* **2019**, *141*, 6680-6689; b) C. Li, C. Zhao, B. Hu, W. Tong, M. Shen, B. Hu, *Chem. Mater.* **2020**, *32*, 1054-1063; c) W. J. Kong, W. Yang, D. Ning, Q. Li, L. Zheng, J. Yang, K. Sun, D. Chen, X. Liu, *Sci. China Mater.* **2020**, *63*, 1703-1718.

[15] E. Marelli, C. Villevieille, S. Park, N. Herault, C. Marino, *ACS Appl. Energy Mater.* **2018**, *1*, 5960-5967.

[16] a) L. Yang, J. M. Lopez del Amo, Z. Shadike, S. M. Bak, F. Bonilla, M. Galceran, P. K. Nayak, J. R. Buchheim, X. Q. Yang, T. Rojo, P. Adelhelm, *Adv. Funct. Mater.* **2020**, *30*, 2003364; b) K. Marker, C. Xu, C. P. Grey, *J. Am. Chem. Soc.* **2020**, *142*, 17447-17456; c) Q. Wang, S. Mariyappan, G. Rousse, A. V. Morozov, B. Porcheron, R. Dedryvere, J. Wu, W. Yang, L. Zhang, M. Chakir, M. Avdeev, M. Deschamps, Y. S. Yu, J. Cabana, M. L. Doublet, A. M. Abakumov, J. M. Tarascon, *Nat. Mater.* **2021**, *20*, 353-361.

[17] a) Y. Xie, E. Gabriel, L. Fan, I. Hwang, X. Li, H. Zhu, Y. Ren, C. Sun, J. Pipkin, M. Dustin, M. Li, Z. Chen, E. Lee, H. Xiong, *Chem. Mater.* **2021**, *33*, 4445-4455; b) J. Xu, D. H. Lee, R. J. Clement, X. Yu, M. Leskes, A. J. Pell, G. Pintacuda, X. Yang, C. P. Grey, Y. Meng, *Chem. Mater.* **2014**, *26*, 1260-1269.

[18] J. H. Park, I. H. Ko, J. Lee, S. Park, D. Kim, S. H. Yu, Y. E. Sung, *ChemElectroChem* **2021**, *8*, 625-643.

[19] W. Kong, R. Gao, Q. Li, W. Yang, J. Yang, L. Sun, X. Liu, *J. Mater. Chem. A* **2019**, *7*, 9099-9109.

[20] a) X. Bai, M. Sathiya, B. Mendoza-Sanchez, A. Iadecola, J. Vergnet, R. Dedryvere, M. Saubanere, A. M. Abakumov, P. Rozier, J.-M. Tarascon, *Adv. Energy Mater.* **2018**, *8*, 1802379; b) X. Rong, J. Liu, E. Hu, Y. Liu, Y. Wang, J. Wu, X. Yu, K. Page, Y. S. Hu, W. Yang, H. Li, X. Q. Yang, L. Chen, X. Huang, *Joule* **2018**, *2*, 125-140.

[21] a) Y. Wang, Z. Feng, P. Cui, W. Zhu, Y. Gong, M.-A. Girard, G. Lajoie, J. Trottier, Q. Zhang, L. Gu, Y. Wang, W. Zuo, Y. Yang, J. B. Goodenough, K. Zaghib, *Nat. Commun.* **2021**, *12*, 13; b) C. Wang, L. Liu, S. Zhao, Y. Liu, Y. Yang, H. Yu, S. Lee, G. H. Lee, Y. M. Kang, R. Liu, F. Li, J. Chen, *Nat. Commun.* **2021**, *12*, 2256.

[22] X. L. Li, T. Wang, Y. Yuan, X. Y. Yue, Q. C. Wang, J. Y. Wang, J. Zhong, R. Q. Lin, Y. Yao, X. J. Wu, X. Q. Yu, Z. W. Fu, Y. Y. Xia, X. Q. Yang, T. Liu, K. Amine, Z. Shadike, Y. N. Zhou, J. Lu, *Adv. Mater.* **2021**, *33*, 2008194.

[23] a) M. Sathiya, J. B. Leriche, E. Salager, D. Gourier, J. M. Tarascon, H. Vezin, *Nat. Commun.* **2015**, *6*, 6276; b) Z. Zhu, H. Wang, Y. Li, R. Gao, X. Xiao, Q. Yu, C. Wang, I. Waluyo, J. Ding, A. Hunt, J. Li, *Adv. Mater.* **2020**, *32*, 2005182.

[24] M. Kalapsazova, S. Ivanova, R. Kukeva, S. Simova, S. Wegner, E. Zhecheva, R. Stoyanova, *Phys. Chem. Chem. Phys.* **2017**, *19*, 27065-27073.

[25] F. Geng, B. Hu, C. Li, C. Zhao, O. Lafon, J. Trebosc, J. P. Amoureux, M. Shen, B. Hu, *J. Mater. Chem. A* **2020**, *8*, 16515-16526.

[26] a) X. Zhang, Y. Qiao, S. Guo, K. Jiang, S. Xu, H. Xu, P. Wang, P. He, H. Zhou, *Adv. Mater.* **2019**, *31*, 1807770; b) Y. Qiao, S. H. Guo, K. Zhu, P. Liu, X. Li, K. Z. Jiang, C. J. Sun, M. W. Chen, H. S.

Zhou, *Energy Environ. Sci.* **2018**, *11*, 299-305.

[27] J. Zhang, Q. Zhang, D. Wong, N. Zhang, G. Ren, L. Gu, C. Schulz, L. He, Y. Yu, X. Liu, *Nat. Commun.* **2021**, *12*, 3071.

[28] a) P. M. Radjenovic, L. J. Hardwick, *Phys. Chem. Chem. Phys.* **2019**, *21*, 1552-1563; b) A. Massaro, A. B. Muñoz-García, P. P. Prosini, C. Gerbaldi, M. Pavone, *ACS Energy Lett.* **2021**, *6*, 2470-2480.

[29] a) J. N. Zhang, Q. Li, C. Ouyang, X. Yu, M. Ge, X. Huang, E. Hu, C. Ma, S. Li, R. Xiao, W. Yang, Y. Chu, Y. Liu, H. Yu, X. Q. Yang, X. Huang, L. Chen, H. Li, *Nat. Energy* **2019**, *4*, 594-603; b) J. Wu, Y. Yang, W. Yang, *Dalton Trans.* **2020**, *49*, 13519-13527; c) E. Hu, Q. Li, X. Wang, F. Meng, J. Liu, J. N. Zhang, K. Page, W. Xu, L. Gu, R. Xiao, H. Li, X. Huang, L. Chen, W. Yang, X. Yu, X.-Q. Yang, *Joule* **2021**, *5*, 720-736.

[30] C. Århammar, A. Pietzsch, N. Bock, E. Holmström, C. M. Araujo, J. Gråsjö, S. Zhao, S. Green, T. Peery, F. Hennies, S. Amerioun, A. Föhlisch, J. Schlappa, T. Schmitt, V. N. Strocov, G. A. Niklasson, D. C. Wallace, J. E. Rubensson, B. Johansson, R. Ahuja, *P. Natl. A. Sci.* **2011**, *108*, 6355-6360.